Langmuir

ARTICLE

pubs.acs.org/Langmuir

Using Stop-Flow Lithography To Produce Opaque Microparticles: Synthesis and Modeling

Su Kyung Suh,[†] Ki Wan Bong,[†] T. Alan Hatton,* and Patrick S. Doyle*

Department of Chemical Engineering, Massachusetts Institute of Technology, Cambridge, Massachusetts 02139, United States

S *Supporting Information*

ABSTRACT: We report on modeling and experimental studies of the synthesis of opaque microparticles made via stop-flow lithography. Opaque magnetic beads and UV-absorbing dyes incorporated into hydrogel microparticles during synthesis changed the height and the degree of cross-linking of the polymer matrices formed. The effect of the concentration of these opaque materials on the particle height was determined experimentally and agreed well with model predictions based on the photopolymerization process over a wide range of UV absorbance. We also created particles with two independent anisotropies, magnetic and geometric, by applying magnetic fields during particle synthesis. Our work provides a platform for rational design of lithographic patterned opaque particles and also a new class of structured magnetic microparticles.

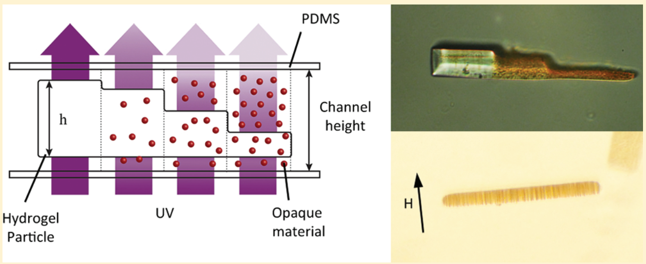

INTRODUCTION

Hydrogels have become increasingly important in tissue engineering,[1] drug delivery,[2] and bioassays,[3] due to their biocompatibility,[4] mechanical stability,[5] responsiveness to environmental cues,[6] controlled degradability,[7] and ease of functionalization.[8] Hydrogels in the form of particles, rather than a bulk substrate, are more attractive in certain applications as they have shorter length scales and can be easily manipulated. Hydrogel particles with spherical or spherelike shapes can be synthesized using bulk emulsion polymerization[9] or two-phase microfluidic systems.[10] Recently, researchers have created various shapes of hydrogel particles using template molding.[11] We had used a different approach, namely stop-flow lithography (SFL), which enables photolithographic particle formation in a semicontinuous operation,[12] with various particle shapes and sizes[13] and with multiple adjacent chemistries.[14] These hydrogel particles can have a variety of chemical functionalities depending on monomer selection and may also contain chemically and/or physically entrapped materials,[15] which can enhance performance for certain applications.

Nanoparticles are also very important materials, since they have large surface-to-volume ratios, can respond to external stimuli quickly, can exhibit interesting properties differing from those of bulk materials,[16] and can be distributed more homogeneously in desired systems than their larger counterparts. Because of these attributes, combinations of hydrogels and nanoparticles have been studied for many applications.[17] This combination is especially interesting when using hydrogel particles, which can have various shapes with further functionalities. Magnetic particles have been used for many applications in imaging,[18] assembly,[19] separation,[20] and applications requiring induced mechanical stress.[21] Efforts to include magnetic materials in hydrogel particles have been accomplished successfully using photolithography.[10b,22] Multifunctional magnetic particles are particularly interesting, as they assist in analyte detection by providing precise control over particles in solution,[22b] color-coding of particles,[22d] and controlled assembly of particles.[22a]

Unfortunately, many of the materials to be embedded in hydrogel particles can inhibit photopolymerization due to their absorbance of the UV light required for the photolysis reaction. We observe this phenomenon during particle synthesis with monomers containing magnetic materials or dyes. In order to better understand this process, and to develop more robust synthesis methods, we investigate here hydrogel particle synthesis with two opaque materials: magnetic beads and a UV-absorbing dye. The latter is used as a model system.

Recently, we investigated the mechanism of the photopolymerization reaction during particle synthesis in PDMS channels.[23] We found that during free-radical polymerization within a channel, oxygen diffuses through the PDMS, scavenging the free radicals and thereby preventing polymerization near the PDMS surfaces. This leaves a lubricating layer of unpolymerized monomer, allowing the particles to flow out of the microfluidic channel easily. We extended our published model describing the reaction process by accounting for the inclusion of opaque materials in the monomer mix and the effect that they have on the depth of penetration of the incident UV radiation and hence on the height of the polymerized hydrogel particles. We also study magnetic particle synthesis with and without an applied uniform magnetic field. Observing and understanding the effects of encapsulated

Received: July 20, 2011
Revised: September 20, 2011
Published: September 26, 2011

© 2011 American Chemical Society

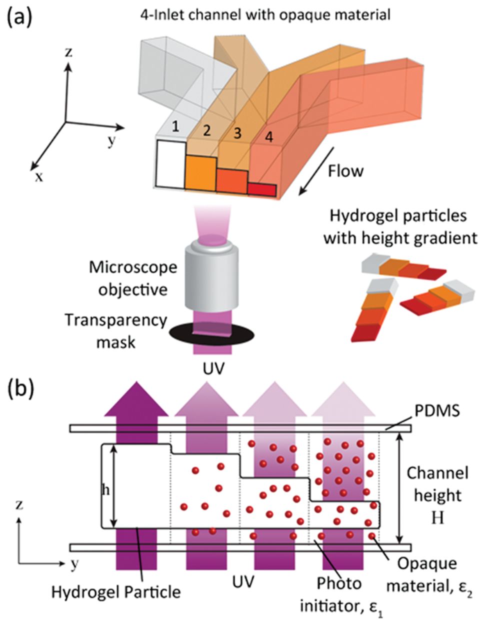

Figure 1. Schematic diagram of a microfluidic channel for stop-flow lithography in the presence of opaque materials.

opaque materials on hydrogel particle height and degree of cross-linking can provide valuable insight into the rational design of new particles with higher degrees of geometric and chemical complexity.

EXPERIMENTAL SECTION

Materials. Polymeric particles are made from poly(ethylene glycol) (700) diacrylate (PEG-DA 700, Sigma-Aldrich) and 2-hydroxy-2-methylpropiophenon (Darocur 1173, Sigma-Aldrich) initiator. We used 100 nm diameter carboxylate-modified magnetic bead solutions (Ademtech) or Allura Red AC (Sigma-Aldrich) solutions as opaque materials. Tween-20 (Sigma-Aldrich) was used at 0.05% to prevent particle loss due to sticking on pipet tips or tubes. To easily observe particle heights, particles were redispersed in 30% (v/v) aqueous solutions of poly(ethylene glycol) (200) (PEG 200, Sigma-Aldrich).

Microfluidic Devices. Microfluidic channels for SFL were fabricated using standard soft-lithography techniques. Polydimethylsiloxane (PDMS, Sylgard 184, Dow Corning) in a 10:1 base-to-curing agent ratio was molded on a patterned silicon wafer (SU-8 photoresist, Microchem) and then cured in an oven at 65 °C for 2 h. Holes for connections to the inlet and outlet were punched with an 18 gauge luer stub adapter. Glass slides were coated with PDMS and partially cured at 65 °C for 22 min. The clean patterned PDMS was assembled with the PDMS-coated glasses and then placed in the oven for 45 min. The prepared microfluidic channel was connected with inlets that were made by pipet tips (ART 10 Reach and ART 200, Molecular BioProducts, Inc.) and outlet aluminum tubing (1/16″, K&S) for collecting particles after synthesis. For particle synthesis, the devices were mounted on the inverted microscope (Axiovert 200, Zeiss).

Stop-Flow-Lithography Setup. We create hydrogel particles in microfluidic devices when flow is stopped. Formed particles are then moved out of the polymerization area via the inflow of fresh monomer solutions. Pulsed flow was operated automatically for the generation of stop-polymerization-flow cycles, alternating the pressure at all four inlets simultaneously from 0 to 3 psi. The relative width of the inlet streams was controlled by a pressure valve (ControlAir, Inc.) and a digital pressure gauge (DPG 100G, Omega Engineering, Inc.). The UV source of Lumen 200 (Prior Scientific, 100% setting) initiated the polymerization reactions. Photomasks were placed in the field-top of the microscope. The desired excitation spectrum was selected using a UV filter (11000v2, Chroma). UV intensity with the 20× objective of an inverted microscope (Axiovert 200, Zeiss) was measured by a UV power meter (Accu-Cal 30, Dymax). All images were taken with a digital SLR camera (D200, Nikon).

Table 1. Simplified Reaction Mechanism in Our Model

reactions	mechanism step
$\mathrm{PI} \xrightarrow{h\nu} \mathrm{R}^{\bullet}$	photolysis
$\mathrm{R}^{\bullet} + \mathrm{M} \rightarrow \mathrm{RM}^{\bullet}$	chain initiation
$\mathrm{RM}_n^{\bullet} + \mathrm{M} \xrightarrow{k_p} \mathrm{RM}_{n+1}^{\bullet}$	chain propagation
$\mathrm{RM}_n^{\bullet} + \mathrm{RM}_m^{\bullet} \xrightarrow{k_t} \mathrm{RM}_n\mathrm{M}_m$	chain termination
$\mathrm{RM}_n^{\bullet} + \mathrm{O}_2 \xrightarrow{k_O} \mathrm{RM}_n\mathrm{OO}$	oxygen inhibition

Particle Synthesis. Figure 1 shows our synthesis procedure. The prepolymer solutions consisted of 5% (v/v) solutions of Darocur 1173, 30% (v/v) PEG-DA 700, and 65% (v/v) opaque material solutions. The concentration of the opaque material solution was adjusted to ensure the desired final concentration of this material in the synthesized hydrogel particles. We generated particles with four distinct chemistries using a microfluidic synthesis device with four inlets. Different concentrations of opaque materials were incorporated in the different regions (Figure 1a); inlet solutions contained 0, 25, 50, and 75 mg/mL magnetic beads in the total prepolymer solutions or 0, 9, 18, and 27 mg/mL UV-absorbing dye. In Allura Red AC prepolymer solutions, 0.01 wt % of methacryloxyethyl thiocarbamoyl rhodamine B (Polysciences, Inc.) was added. After the synthesis, unreacted monomer solution was removed by rinsing particles with Tween-20 solutions.

UV Absorbance Measurement. UV absorption measurements were performed with a UV−vis spectrometer (HP 8453, Hewlett-Packard). To measure highly concentrated solutions, we used quartz cuvettes with 0.1 mm path length (Starna Cells, Inc.). Each sample was measured five times, and five samples were taken for each concentration. The UV absorbance at 365 nm (wavelength used for polymerization) was recorded.

Particle Height Measurement. Bright field was used to image magnetic particles, while particles synthesized with the UV-absorbing dye were observed with fluorescence microscopy. Particle heights were measured using Image J software. Straight lines were drawn throughout particle height cross sections, and pixel intensity was plotted as a function of distance along the lines. The edges of the particles were well-defined for magnetic particles. For particles created with the dye, we measured fluorescence intensity, defining particle heights when the fluorescent signal is 3 times higher than noise (S/N = 3).

Magnetic Characterization. Uniform magnetic fields were generated using a custom-made electromagnet with a dc power supply (GPS-2303, GW Instek). The induced magnetic field strength was measured with a gauss meter (SYPRIS).

MODEL DESCRIPTION

Governing Equations. We developed a one-dimensional model to describe particle synthesis in flow lithography, including photolysis, chain initiation, chain propagation, chain termination, and inhibition in the reaction mechanism as listed in

Table 1. We build off our prior modeling efforts which did not consider UV absorbance.[23]

We based this model on our previous work, modifying it to allow also for the effect of the UV-absorbing materials. Figure 1b shows the channel geometry, illustrating UV absorption caused by both photoinitiator and magnetic beads. The light intensity $I(z)$ can be expressed by the following equation, assuming that the two materials absorb UV light independently.

$$\frac{\partial I(z)}{\partial z} = -(\varepsilon_1[\mathrm{PI}] + \varepsilon_2[\mathrm{OM}])I(z) \qquad (1)$$

$$I(z) = I_0 \exp(-(\varepsilon_1[\mathrm{PI}] + \varepsilon_2[\mathrm{OM}])z) \qquad (2)$$

where ε_1 and ε_2 are the extinction coefficients of the photoinitiator and the magnetic beads or dye, respectively, at a wavelength of 365 nm. [PI] and [OM] represent concentrations of photoinitiator and magnetic beads or dye, respectively. I_0 is the UV intensity at $z = 0$. Since the rate of radical production, r_a, within dz is proportional to the volumetric UV absorption rate by the photoinitiator,

$$r_a = -\varphi\frac{\varepsilon_1[\mathrm{PI}]}{\varepsilon_1[\mathrm{PI}] + \varepsilon_2[\mathrm{OM}]}\frac{\partial I(z)}{\partial z} \qquad (3)$$

$$r_a = \varphi I_0 \varepsilon_1[\mathrm{PI}] \exp(-(\varepsilon_1[\mathrm{PI}] + \varepsilon_2[\mathrm{OM}])z) \qquad (4)$$

where φ is the quantum yield of formation of initiating radicals. All the radicals listed in Table 1 were lumped into a single term, $X^\bullet$, in our model. The radical consumption rate, r_c, can be expressed as the summation of chain propagation and termination rates

$$r_c = k_t[X^\bullet]^2 + k_O[X^\bullet][O_2] \qquad (5)$$

Using the quasi-steady-state approximation, $r_a = r_c$, we derived the expression

$$[X^\bullet] = \frac{-k_O[O_2] + \sqrt{(k_O[O_2])^2 + 4r_a k_t}}{2k_t} \qquad (6)$$

where $[O_2]$ is the concentration of oxygen, and k_t and k_O are the rate constant for chain termination and oxygen inhibition, respectively. The concentration of monomer, [M], and $[O_2]$ are expressed below as functions of z and time, t, using the mass transport equation. Diffusion of monomers was not considered here, as they are relatively large compared to oxygen.

$$\frac{\partial[O_2]}{\partial t} = D_O\frac{\partial^2[O_2]}{\partial z^2} - k_O[O_2][X^\bullet] \qquad (7)$$

$$\frac{\partial[M]}{\partial t} = -k_p[M][X^\bullet] \qquad (8)$$

Nondimensionalizing eqs 7 and 8 using

$$\tau = tD_O/H^2,\ \theta = [O_2]/[O_{2,\mathrm{eqb}}],\ \eta = z/H,\ \xi[M]/[M_0]$$

$$\mathrm{Da}_1 = \frac{K_O{}^2H^2[O_{2,\mathrm{eqb}}]}{2k_tD_O},\ \mathrm{Da}_2 = \frac{k_pk_O[O_{2,\mathrm{eqb}}]H^2}{2k_tD_O},$$

$$\alpha = \frac{4\varphi\varepsilon[\mathrm{PI}]I_0k_t}{k_O{}^2[O_{2,\mathrm{eqb}}]^2},\ \beta = (\varepsilon_1[\mathrm{PI}] + \varepsilon_2[\mathrm{OM}])H$$

we obtain the equations

$$\frac{\partial\theta}{\partial\tau} = \frac{\partial^2\theta}{\partial\eta^2} - \mathrm{Da}_1\theta(-\theta + \sqrt{\theta^2 + \alpha\exp(-\beta\eta)}) \qquad (9)$$

$$\frac{\partial\xi}{\partial\tau} = \mathrm{Da}_2\xi(-\theta + \sqrt{\theta^2 + \alpha\exp(-\beta\eta)}) \qquad (10)$$

where $[O_{2,\mathrm{eqb}}]$ is the equilibrium oxygen concentration, $[M_0]$ is the initial oligomer concentration, D_O is the diffusivity of oxygen in oligomer solutions, k_p is the rate constant for chain propagation, and H is the channel height. The dimensionless parameter β includes the effects of additional UV-absorbing materials present during synthesis. Using the parameter values listed in Table 2, the resulting values of the dimensionless groups Da_1, Da_2, and α are 6×10^8, 3×10^4, and 6×10^{-7}, respectively.

Table 2. Parameters Used in This Paper

parameters	value	unit	reference
k_p	25	m^3/mol s	24
k_t	2520	m^3/mol s	24
k_O	5×10^5	m^3/mol s	25
H	30	μm	measured
I_0	3400	mW/cm^2	measured
[PI]	329	mol/m^3	measured
ε_1	1.6	m^3/mol m	26
$[O_{2,\mathrm{eqb}}]$	1.5	mol/m^3	27
φ	0.6	unitless	26

Boundary and Initial Conditions. The initial and boundary conditions are

$$\theta(0,\tau) = 1\ \theta(1,\tau) = 1\ \theta(\eta,0) = 1\ \xi(\eta,0) = 1$$

Numerical Solution. To solve the equations, we used the method of lines with MATLAB solver ode15s, discretizing eqs 9 and 10 in the η direction. The simulations were run with 400 uniform mesh elements in the η-direction, and a maximum dimensionless time step of 10^{-6}.

RESULTS AND DISCUSSION

To study the effect of loading on polymerization, we introduced four monomer solutions with different magnetic particle concentrations as separate streams in parallel coflow to the microfluidics channel, as shown in Figures 1a and 2a. Upon irradiation, the regions with higher concentrations of magnetic beads absorbed UV light more strongly than did those with lower bead concentrations and therefore had the lowest UV intensities at the top of the channel, where $z = H$ (Figure 1b). This UV intensity variation across the channel can be seen in Figure 2d as a variation in the strength of the fluorescence emission from fluorescent blue beads spread on the top of the channel and excited at their excitation wavelength of 360 nm. The color changes across the channel correspond to the changes in UV penetration through each region of the monomer stream. The hydrogel particles formed under these conditions were stepped in height, reflecting the variations in transmitted UV illumination and in free radical generation required to initiate the polymerization reaction. Fewer radicals initiate fewer polymerization reactions and lead to regions where the conversion is less than the gel point and the weakly cross-linked polymers are then

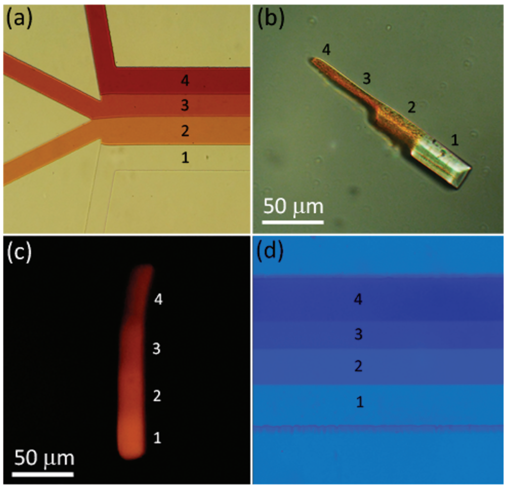

Figure 2. (a) Bright-field image of a four-inlet microfluidic channel having 0, 25, 50, and 75 mg/mL magnetic bead monomer solutions. (b) Side view of a particle synthesized in the channel depicted in part a. (c) Fluorescent side view image of a particle created with a UV-absorbing dye (Allura Red AC), where the prepolymer solutions contained 0, 9, 18, 27 mg/mL of dye labeled 1, 2, 3, 4 on the particle, respectively. (d) Fluorescent beads with an excitation wavelength of 360 nm and an emission wavelength of 407 nm were spread on the top of channel. The UV projected from the objective passes through the monomer solutions to excite the blue bead-coated substrate and the emission from the beads travels back through the sample, where it is then captured by the objective for detection. The light intensity from the fluorescent beads depends on the concentration of magnetic beads in the channel.

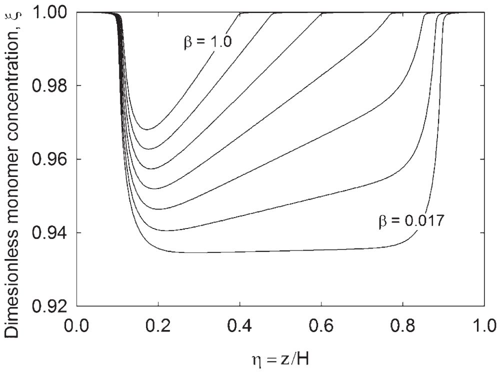

Figure 3. Un-cross-linked monomer concentration (ξ) profile between the bottom ($\eta = 0$) and the top ($\eta = 1$) of the channel for various values of β (0.017, 0.17, 0.34, 0.51, 0.68, 0.85, 1.0). These results were obtained numerically by solving eqs 9 and 10.

washed away during the particle recovery processes. As shown in Figure 2b, the synthesized magnetic particles showed a stepped height and color profile, since a different concentration of magnetic beads was incorporated in each region of the particles.

Likewise, we studied particles generated in the presence of a UV-absorbing dye, again using four flow regions, but with different dye concentrations rather than magnetic beads. In Figure 2c, we observe variations in both the heights and fluorescence intensities along the particle, demonstrating that a height gradient can also result from particle synthesis with monomers containing materials other than UV-absorbing beads. Importantly, these UV-absorbing dyes need not be incorporated permanently in the resulting particles, since they can be washed out after synthesis. Therefore, one can use UV-absorbing dye solutions as in situ flow masks.[28]

To understand better this phenomenon, we implemented our model described above. Simulation results for monomer conversion ξ as a function of position η in the synthesis channel are shown in Figure 3 for different values of the parameter β, an effective UV absorption coefficient accounting for both the photoinitiator and the UV-absorbing materials. At $\xi = 0.98$, taken to be the critical conversion factor at which the gel first begins to form,[29] the particle height decreases as β increases, and the position at which gelation first occurs is the same regardless of β. These results are consistent with the experimental observations; particles synthesized with the magnetic beads have a flat surface at the bottom and a stairlike profile on the far side of the light source (Figure 2b), rather than the symmetric tapered shape about the $x-y$ plane usually observed in the absence of absorbing additives. The fluorescent image for particles synthesized with the dye (Figure 2c), on the other hand, does not have readily distinguishable boundaries in the bright-field image, which can also be explained with our model. As β increases, the slope ($d\xi/d\eta$) near $\eta = 1$ decreases. Since there is a relatively wide region where $\xi = 0.98$, it is difficult to visualize distinct boundaries in the polymer matrix. However, the fluorescent signal from the incorporated rhodamine enables us to observe the boundary more readily. It should also be noted that monomer conversion along the direction η is not constant, creating a nonuniform polymer matrix. This ability to create particles with a monomer conversion gradient in the z-direction provides a means to control the third dimension of particle morphology during synthesis: particle shape and chemistry can be dictated in the x and y directions by varying inlet flows and transparency mask shapes, while UV-absorbing dyes can be used to control height and monomer conversion in the z-direction.

Figure 4a compares the normalized particle heights obtained experimentally with the simulation predictions as a function of β. The simulation heights were estimated by selecting the region $\xi < 0.98$ to be the cross-linked particle network, while the particle heights were determined experimentally by observing optical images. In general, particles synthesized in the presence of the UV-absorbing dye had difficult-to-distinguish boundaries, as discussed above, and hence heights for these particles were delineated by fluorescence intensity measurements. UV—vis spectrometry was employed to measure the UV absorbances of the magnetic beads and the UV-absorbing dye; dilute conditions, 25 mg/mL for the magnetic bead suspension and 9 mg/mL for the dye solution, with a path length of 0.1 mm, were used in these measurements. The absorbance at higher concentrations was obtained by extrapolating from the low-concentration measurements. Further details of these experiments including particle height measurements can be found in the Supporting Information. While the comparison between experimental and predicted results is good over the whole range of β-values studied, the experimental results for particles with relatively low β are in particularly good agreement with the simulation predictions. The success of our model-based height predictions suggests that we can estimate the particle heights that would be obtained with any given magnetic bead or dye concentration. With magnetic particles, in particular, where the loading of magnetic beads determines the particle magnetic response characteristics, it is important to be able to optimize the trade-off between increased magnetic bead concentration and the decreased particle height,

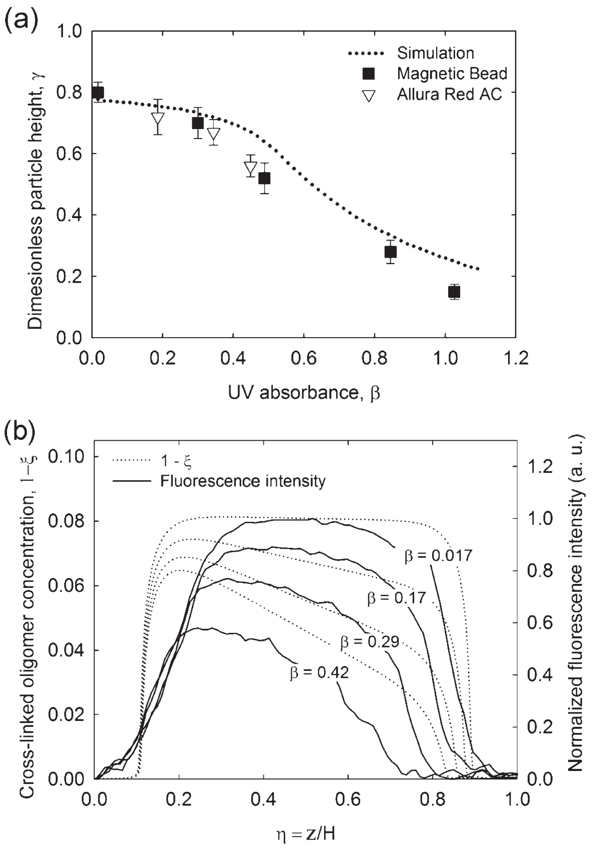

Figure 4. Comparison of experimental data and modeling results. (a) Dimensionless particle height γ (scaled by channel height) versus UV absorbance β. Dotted line is from simulations. Solid squares and open triangles are from experiments using magnetic beads and UV-absorbing dye, respectively. (b) Cross-linked oligomer concentration ($1 - \xi$, shown as dotted lines and acquired from simulation) versus dimensionless height in channel η. Right axis and solid curves show for comparison the fluorescent signals across the η-direction, as acquired from particles synthesized in the presence of UV-absorbing dye.

since their product determines the total magnetic response of the particle. In our case, a concentration of 50 mg/mL leads to the maximum total magnetic bead loading in the particles. Another consideration in the selection of the initial magnetic bead concentration is that the decreased height that results in regions with high magnetic loading can lead to mechanical instability in the particle architecture. Similar arguments hold for the particles based on UV-absorbing dyes which can be designed to provide suitable optical characteristics. The model developed here provides important criteria for the design of particles with desired magnetic or optical properties.

In addition to providing predictions on the effects of absorbing materials on the morphologies of particles prepared by SFL, the model developed here can also provide insights into the cross-linking densities in the polymer network. Experimentally determined fluorescence intensity profiles across each of the four sections of the particle shown in Figure 2c, corresponding to the four different UV-absorbing dye concentrations used, are plotted using solid lines. Simulation results using the β-values appropriate for each of the UV dye concentrations in our experiments are shown as broken lines for comparison with the experimentally derived profiles. The agreement is good, although the fluorescent signal profiles do not exhibit edges as sharp as those in the simulations near $\eta = 0.1$ and 0.9, but they are consistent with the simulations in terms of relative intensities and internal slopes over the internal position range $0.3 < \eta < 0.7$.

We have identified two potential explanations for the discrepancies between the simulation results and the experimental profiles at the top and bottom edges of the particles. First, the simulation of particle formation does not take into account swelling effects after particle synthesis. The lower the cross-linking density of a gel network, the more likely it is that the network will swell in a solvent. The gradient in the cross-link density across the particle when it is prepared in the presence of UV-absorbing entities should then result in the particle swelling to different extents within the particle. The second reason is that we used rhodamine B bearing a methacrylate group in order to incorporate it covalently within the gel. The assumption behind Figure 4b is that the rhodamine incorporation rate in the four cases is the same, providing an estimate of the relative cross-linked monomer concentrations. However, the reaction rate of rhodamine could depend on the local concentration of free radicals, which is not taken into account for this species in the model. This may explain why the results for the particle region with 45 mg/mL of dye concentration do not agree with our model predictions as well as they do for other concentrations. We believe that Figure 4b provides useful information on hydrogel particle synthesis with nonfunctionalizing UV-absorbing materials, given the limited set of assumptions applied.

To better understand the effects of magnetic bead distribution within the monomers during polymerization, we performed an experiment under an applied uniform magnetic field directed normal to the observation plane (Figure 5) to assemble the magnetic particles in chains in the same direction in which light propagates through the monomer. This provided bead-free spaces for light penetration through to the top of the channel (Figure 5a). Our hypothesis was that nearby free radicals would polymerize around magnetic chains due to slight free radical diffusion. Magnetic beads in the monomer solution were chained in the microfluidic channel with spaces between chains and particles polymerized as in other syntheses, as shown in Figure 5b. As expected, the height of the particle prepared under a uniform magnetic field (0.76H) was larger than that in the absence of the magnetic field (0.69H). This trend can be discerned qualitatively in Figure 5c−f. The dimensionless particle height of 0.76 with the chained beads was very close to the expected value of 0.78 predicted in the simulation with $\beta = 0.017$; i.e., the value obtained when no opaque material was added. In this case, the microscopic or local UV absorbance in the channels between the chains determined the particle height and the degree of cross-linking, rather than total absorbance averaged over the entire particle. Additionally, because it is the local absorbance between the chains that largely determines the overall particle thickness, chaining of the beads allows us to create thicker particles compared to randomly dispersed beads under the same synthesis conditions.

We next applied a magnetic field to flip the particles on their edges, so that they could be observed from their sides. Interestingly, the direction of the magnetic field required to flip the particle for height observation was different for particles with chained magnetic beads than for those with homogenously distributed magnetic beads. Magnetic particles align with a field based on the most energetically favorable orientation; therefore, in the case of particles generated in the presence of a field, the

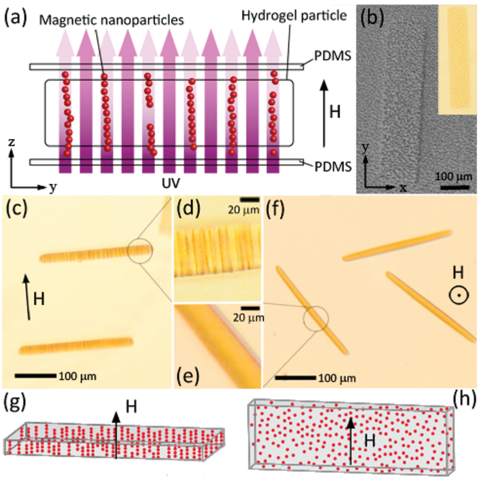

Figure 5. Particles synthesized in the presence of an external magnetic field. (a) A uniform magnetic field was applied just before UV exposure to form chained magnetic beads. Although the chains absorb UV, microparticles can be created due to polymerization near and around the chains (shown schematically as purple in the image). (b) Top view of the microfluidic channel with 25 mg/mL magnetic beads during the synthesis. The inset image is a washed particle after the synthesis. (c) Particles with magnetic chains embedded. A uniform magnetic field was applied to orient the particles for more convenient observation of the chains. (d, e) Magnified image of the circled part of parts c and f, respectively. (f) Particles with 25 mg/mL magnetic beads synthesized with no magnetic field present. (g, h) Illustration of particle alignment under the magnetic field. The particle in part g contains chained magnetic beads, while the particle in part h has embedded randomly distributed magnetic beads. These particles orient differently under the same magnetic field.

already chained magnetic beads aligned with the field, while for homogeneously distributed beads, it was the entire hydrogel particle that aligned with the field, as shown experimentally in Figure 5c−f and schematically in Figure 5g,h. These figures represent particle alignment under weak fields; with stronger fields, the particles would overcome the forces of gravity and align along their longest axes. Although particle synthesis in the presence of external magnetic fields has been reported by other groups,[22d,30] the significance of our work is that the particle synthesis approach allows for independent control over its geometric and magnetic anisotropies. This enables the assembly of magnetic particles in a desired orientation, regardless of geometric anisotropy, and provides the ability to create anisotropies in many other functional particles, including mechanical strength, dielectric constant, and elasticity. Furthermore, we believe that our work can lead to a new method to fabricate phononic particles by applying an external electric field.

We have discussed the effect of opaque materials on the synthesis of hydrogel microparticles and have demonstrated how the understanding gained in this work can be applied to the design of new types of such particles. In particular, the effective functionalization of hydrogel particles through the incorporation of nanoparticles depends on the UV absorptivity of the incorporated material, published values of which have been collected in Table S2 of the Supporting Information as a function of material, size, and wavelength. When nanoparticles of high UV absorbance are to be incorporated, an external field can often be used to create patterns in the monomer solutions and allow for increased local UV intensities in the particle free zones. This allows for improved reaction rates over the particle height and enhanced properties of the resulting hydrogels. In the presence of an external field, then, ε_2 should be the UV absorptivity of the reaction solution itself rather than that of the bulk suspension.

■ CONCLUSION

In summary, we demonstrate the synthesis of opaque hydrogel particles using flow-lithography, where the heights of the particles are determined by the depth of penetration of the initiating UV light sources. The properties of the particles such as variation in cross-linking densities across the particles and their heights are well-described by a reformulation of an earlier model published by our group. The insights gained from this approach enabled the design of new particle architectures with two independent anisotropies by using magnetic beads chained under a uniform magnetic field during synthesis. This study advances the understanding of the synthesis of a diverse class of particles with variable shape, chemistry, and functionality. We believe that our model and new synthesis techniques with opaque materials can lead to rational particle design with minimal experimentation.

■ ASSOCIATED CONTENT

Ⓢ **Supporting Information.** Additional information as noted in the text. This material is available free of charge via the Internet at http://pubs.acs.org.

■ AUTHOR INFORMATION

Corresponding Author

*E-mail: pdoyle@mit.edu (P.S.D.), tahatton@mit.edu (T.A.H.).

Author Contributions

†These authors contributed equally to this work.

■ ACKNOWLEDGMENT

This work was supported by Singapore-MIT Alliance and NSF grant DMR-1006147.

■ REFERENCES

(1) Cushing, M. C.; Anseth, K. S. Hydrogel cell cultures. *Science* **2007**, *316* (5828), 1133–1134.

(2) Peppas, N. A.; Hilt, J. Z.; Khademhosseini, A.; Langer, R. Hydrogels in biology and medicine: From molecular principles to bionanotechnology. *Adv. Mater.* **2006**, *18* (11), 1345–1360.

(3) Ulijn, R. V.; Bibi, N.; Jayawarna, V.; Thornton, P. D.; Todd, S. J.; Mart, R. J.; Smith, A. M.; Gough, J. E. Bioresponsive hydrogels. *Mater. Today* **2007**, *10* (4), 40–48.

(4) Lee, K. Y.; Mooney, D. J. Hydrogels for tissue engineering. *Chem. Rev.* **2001**, *101* (7), 1869–1879.

(5) Malkoch, M.; Vestberg, R.; Gupta, N.; Mespouille, L.; Dubois, P.; Mason, A. F.; Hedrick, J. L.; Liao, Q.; Frank, C. W.; Kingsbury, K.; Hawker, C. J. Synthesis of well-defined hydrogel networks using click chemistry. *Chem. Commun.* **2006**, No. 26, 2774–2776.

(6) Nath, N.; Chilkoti, A. Creating "smart" surfaces using stimuli responsive polymers. *Adv. Mater.* **2002**, *14* (17), 1243–1247.

(7) Anseth, K. S.; Metters, A. T.; Bryant, S. J.; Martens, P. J.; Elisseeff, J. H.; Bowman, C. N. In situ forming degradable networks and their application in tissue engineering and drug delivery. *J. Controlled Release* **2002**, *78* (1−3), 199–209.

(8) Kawaguchi, H. Functional polymer microspheres. *Prog. Polym. Sci.* **2000**, *25* (8), 1171–1210.

(9) Smith, W. V.; Ewart, R. H. Kinetics of emulsion polymerization. *J. Chem. Phys.* **1948**, *16* (6), 592–599.

(10) (a) Dendukuri, D.; Tsoi, K.; Hatton, T. A.; Doyle, P. S. Controlled synthesis of nonspherical microparticles using microfluidics. *Langmuir* **2005**, *21* (6), 2113–2116. (b) Hwang, D. K.; Dendukuri, D.; Doyle, P. S. Microfluidic-based synthesis of non-spherical magnetic hydrogel microparticles. *Lab Chip* **2008**, *8* (10), 1640–1647. (c) Shepherd, R. F.; Conrad, J. C.; Rhodes, S. K.; Link, D. R.; Marquez, M.; Weitz, D. A.; Lewis, J. A. Microfluidic assembly of homogeneous and janus colloid-filled hydrogel granules. *Langmuir* **2006**, *22* (21), 8618–8622. (d) Xu, S.; Nie, Z.; Seo, M.; Lewis, P.; Kumacheva, E.; Stone, H. A.; Garstecki, P.; Weibel, D. B.; Gitlin, I.; Whitesides, G. M. Generation of monodisperse particles by using microfluidics: Control over size, shape, and composition. *Angew. Chem., Int. Ed.* **2005**, *117* (5), 734–738. (e) Kumacheva, E.; Garstecki, P. *Microfluidic Reactors for Polymer Particles*; Wiley: Hoboken, NJ, 2011.

(11) Rolland, J. P.; Maynor, B. W.; Euliss, L. E.; Exner, A. E.; Denison, G. M.; DeSimone, J. M. Direct fabrication and harvesting of monodisperse, shape-specific nanobiomaterials. *J. Am. Chem. Soc.* **2005**, *127* (28), 10096–10100.

(12) (a) Dendukuri, D.; Pregibon, D. C.; Collins, J.; Hatton, T. A.; Doyle, P. S. Continuous-flow lithography for high-throughput microparticle synthesis. *Nat. Mater.* **2006**, *5* (5), 365–369. (b) Dendukuri, D.; Gu, S. S.; Pregibon, D. C.; Hatton, T. A.; Doyle, P. S. Stop-flow lithography in a microfluidic device. *Lab Chip* **2007**, *7* (7), 818–828.

(13) Haghgooie, R.; Toner, M.; Doyle, P. S. Squishy non-spherical hydrogel microparticles. *Macromol. Rapid Commun.* **2010**, *31* (2), 128–134.

(14) Bong, K. W.; Bong, K. T.; Pregibon, D. C.; Doyle, P. S. Hydrodynamic focusing lithography. *Angew. Chem. Int. Ed.* **2010**, *49* (1), 87–90.

(15) (a) Pregibon, D. C.; Toner, M.; Doyle, P. S. Multifunctional encoded particles for high-throughput biomolecule analysis. *Science* **2007**, *315* (5817), 1393–1396. (b) Shepherd, R. F.; Panda, P.; Bao, Z.; Sandhage, K. H.; Hatton, T. A.; Lewis, J. A.; Doyle, P. S. Stop-flow lithography of colloidal, glass, and silicon microcomponents. *Adv. Mater.* **2008**, *20* (24), 4734–4739. (c) Panda, P.; Ali, S.; Lo, E.; Chung, B. G.; Hatton, T. A.; Khademhosseini, A.; Doyle, P. S. Stop-flow lithography to generate cell-laden microgel particles. *Lab Chip* **2008**, *8* (7), 1056–1061. (d) Appleyard, D. C.; Chapin, S. C.; Doyle, P. S. Multiplexed protein quantification with barcoded hydrogel microparticles. *Anal. Chem.* **2011**, *83* (1), 193–199. (e) Chapin, S. C.; Pregibon, D. C.; Doyle, P. S. Rapid microRNA profiling on encoded gel microparticles. *Angew. Chem. Int. Ed.* **2011**, *50* (10), 2289–2293.

(16) Murray, C. B.; Kagan, C. R.; Bawendi, M. G. Synthesis and characterization of monodisperse nanocrystals and close-packed nanocrystal assemblies. *Annu. Rev. Mater. Sci.* **2000**, *30*, 545–610.

(17) (a) Im, J. S.; Bai, B. C.; In, S. J.; Lee, Y. S. Improved photodegradation properties and kinetic models of a solar-light-responsive photocatalyst when incorporated into electrospun hydrogel fibers. *J. Colloid Interface Sci.* **2010**, *346* (1), 216–221. (b) Li, J.; Hong, X.; Liu, Y.; Li, D.; Wang, Y. W.; Li, J. H.; Bai, Y. B.; Li, T. J. Highly photoluminescent CdTe/Poly(*N*-isopropylacrylamide) temperature-sensitive gels. *Adv. Mater.* **2005**, *17* (2), 163–166.

(18) Pankhurst, Q. A.; Connolly, J.; Jones, S. K.; Dobson, J. Applications of magnetic nanoparticles in biomedicine. *J. Phys. D Appl. Phys.* **2003**, *36* (13), R167–R181.

(19) (a) Isojima, T.; Suh, S. K.; Vander Sande, J. B.; Hatton, T. A. Controlled assembly of nanoparticle structures: Spherical and toroidal superlattices and nanoparticle-coated polymeric beads. *Langmuir* **2009**, *25* (14), 8292–8298. (b) Harada, T.; Hatton, T. A. Formation of highly ordered rectangular nanoparticle superlattices by the cooperative self-assembly of nanoparticles and fatty molecules. *Langmuir* **2009**, *25* (11), 6407–6412. (c) Singh, H.; Laibinis, P. E.; Hatton, T. A. Synthesis of flexible magnetic nanowires of permanently linked core−shell magnetic beads tethered to a glass surface patterned by microcontact printing. *Nano Lett.* **2005**, *5* (11), 2149–2154. (d) Zerrouki, D.; Baudry, J.; Pine, D.; Chaikin, P.; Bibette, J. Chiral colloidal clusters. *Nature* **2008**, *455* (7211), 380–382. (e) Chen, C. H.; Abate, A. R.; Lee, D. Y.; Terentjev, E. M.; Weitz, D. A. Microfluidic assembly of magnetic hydrogel particles with uniformly anisotropic structure. *Adv. Mater.* **2009**, *21* (31), 3201–3204.

(20) (a) Bucak, S.; Jones, D. A.; Laibinis, P. E.; Hatton, T. A. Protein separations using colloidal magnetic nanoparticles. *Biotechnol. Prog.* **2003**, *19* (2), 477–484. (b) Moeser, G. D.; Roach, K. A.; Green, W. H.; Hatton, T. A.; Laibinis, P. E. High-gradient magnetic separation of coated magnetic nanoparticles. *Aiche J.* **2004**, *50* (11), 2835–2848. (c) Gerber, R.; Birss, R. R. *High Gradient Magnetic Separation*; Research Studies Press: Chichester, NY, 1983; (d) Yavuz, C. T.; Mayo, J. T.; Yu, W. W.; Prakash, A.; Falkner, J. C.; Yean, S.; Cong, L. L.; Shipley, H. J.; Kan, A.; Tomson, M.; Natelson, D.; Colvin, V. L. Low-field magnetic separation of monodisperse Fe_3O_4 nanocrystals. *Science* **2006**, *314* (5801), 964–967.

(21) (a) Dreyfus, R.; Baudry, J.; Roper, M. L.; Fermigier, M.; Stone, H. A.; Bibette, J. Microscopic artificial swimmers. *Nature* **2005**, *437* (7060), 862–865. (b) Zhang, L.; Abbott, J. J.; Dong, L. X.; Kratochvil, B. E.; Bell, D.; Nelson, B. J. Artificial bacterial flagella: Fabrication and magnetic control. *Appl. Phys. Lett.* **2009**, *94* (6), 064107. (c) Ghosh, A.; Fischer, P. Controlled propulsion of artificial magnetic nanostructured propellers. *Nano Lett.* **2009**, *9* (6), 2243–2245.

(22) (a) Yuet, K. P.; Hwang, D. K.; Haghgooie, R.; Doyle, P. S. Multifunctional superparamagnetic janus particles. *Langmuir* **2010**, *26* (6), 4281–4287. (b) Bong, K. W.; Chapin, S. C.; Doyle, P. S. Magnetic barcoded hydrogel microparticles for multiplexed detection. *Langmuir* **2010**, *26* (11), 8008–8014. (c) Kim, H.; Ge, J.; Kim, J.; Choi, S.; Lee, H.; Lee, H.; Park, W.; Yin, Y.; Kwon, S. Structural colour printing using a magnetically tunable and lithographically fixable photonic crystal. *Nat. Photonics* **2009**, *3* (9), 534–540. (d) Lee, H.; Kim, J.; Kim, H.; Kim, J.; Kwon, S. Colour-barcoded magnetic microparticles for multiplexed bioassays. *Nat. Mater.* **2010**, *9* (9), 745–749.

(23) Dendukuri, D.; Panda, P.; Haghgooie, R.; Kim, J. M.; Hatton, T. A.; Doyle, P. S. modeling of oxygen-inhibited free radical photopolymerization in a PDMS microfluidic device. *Macromolecules* **2008**, *41* (22), 8547–8556.

(24) Kızılel, S.; Pérez Luna, V. H.; Teymour, F. Mathematical model for surface initiated photopolymerization of poly(ethylene glycol) diacrylate. *Macromol. Theory Simul.* **2006**, *15* (9), 686–700.

(25) Decker, C.; Jenkins, A. D. Kinetic approach of oxygen inhibition in ultraviolet-and laser-induced polymerizations. *Macromolecules* **1985**, *18* (6), 1241–1244.

(26) Lecamp, L.; Lebaudy, P.; Youssef, B.; Bunel, C. Influence of UV radiation wavelength on conversion and temperature distribution profiles within dimethacrylate thick material during photopolymerization. *Polymer* **2001**, *42* (21), 8541–8547.

(27) Goodner, M. D.; Bowman, C. N. Development of a comprehensive free radical photopolymerization model incorporating heat and mass transfer effects in thick films. *Chem. Eng. Sci.* **2002**, *57* (5), 887–900.

(28) Chen, C. C.; Hirdes, D.; Folch, A. Gray-scale photolithography using microfluidic photomasks. *Proc. Natl. Acad. Sci. U. S. A.* **2003**, *100* (4), 1499–1504.

(29) Andrzejewska, E. Photopolymerization kinetics of multifunctional monomers. *Prog. Polym. Sci.* **2001**, *26* (4), 605–665.

(30) (a) Dyab, A. K. F.; Ozmen, M.; Ersoz, M.; Paunov, V. N. Fabrication of novel anisotropic magnetic microparticles. *J. Mater. Chem.* **2009**, *19* (21), 3475–3481. (b) Seiffert, S.; Romanowsky, M. B.; Weitz, D. A. Janus microgels produced from functional precursor polymers. *Langmuir* **2010**, *26* (18), 14842–14847. (c) Nunes, J.; Herlihy, K. P.; Mair, L.; Superfine, R.; DeSimone, J. M. Multifunctional shape and size specific magneto-polymer composite particles. *Nano Lett.* **2010**, *10* (4), 1113–1119. (d) Kim, S. H.; Sim, J. Y.; Lim, J. M.; Yang, S. M. Magnetoresponsive microparticles with nanoscopic surface structures for remote-controlled locomotion. *Angew. Chem. Int. Ed.* **2010**, *49* (22), 3786–3790.